Onset of thin film meniscus along a fiber

SHUO GUO,[1] XIANMIN XU,[2] TIEZHENG QIAN,[3]
YANA DI,[2] MASAO DOI[4] AND PENGER TONG[1]

[1]Department of Physics, Hong Kong University of Science and Technology,
Clear Water Bay, Kowloon, Hong Kong
[2]LSEC, Institute of Computational Mathematics and Scientific/Engineering Computing,
AMSS, NCMIS, Chinese Academy of Sciences, Beijing 100080, China
[3]Department of Mathematics, Hong Kong University of Science and Technology,
Clear Water Bay, Kowloon, Hong Kong
[4]Interdisciplinary Research Center, Beihang University, Beijing 100191, China

The dynamics of spreading of a macroscopic liquid droplet over a wetting surface is often described by a power-law relaxation, which is known as Tanner's law. Here we report a combined experimental and theoretical study on how a freely suspended soap film wets and spreads along a micron-sized glass fiber in contact with the soap film. When the film thickness ℓ becomes smaller than the fiber diameter d, the strong hydrodynamic confinement effect of the soap film gives rise to a logarithmic relaxation with fiber draining time t. Such a slow dynamics of spreading is observed for hours both in the measured time-dependent height of capillary rise $h(t)$ on the fiber surface and viscous friction coefficient $\xi_s(t)$ felt by the glass fiber in contact with a soap film. A new theoretical approach based on the Onsager variational principle is developed to describe the dynamics of thin film spreading along a fiber. The newly derived equations of motion provide the analytical solutions of $h(t)$ and contact angle $\theta(t)$, which are found to be in good agreement with the experimental results. Our work thus provides a common framework for understanding the confinement effect of thin soap films in the dynamics of spreading along a fiber.

1. Introduction

Spreading of a liquid droplet over a flat or curved surface is a common phenomenon in nature and technology, which is relevant to many practical applications ranging from spreading of droplets, lubricants, and coatings to microfluidic devices, inkjet printing and the extraction of oil from sandstone by injecting water or gas (Bonn *et al.* 2013; Snoeijer & Andreotti 2013). Droplet spreading over an ambient solid surface is complicated and not well understood, because it involves the motion of a contact line (CL) at the edge of the spreading droplet. A moving CL between the liquid interface and solid surface is incompatible with the non-slip boundary condition and would lead to unphysical infinite dissipation (Dussan & Davis 1974). As a classical example of the moving CL problem, droplet spreading is an outstanding problem in interfacial dynamics and has been with us for many years (de Gennes 1985; Leger & Joannyde 1992; Decker & Garoff 1997; Quéré 2008; Bonn *et al.* 2013; Snoeijer & Andreotti 2013; Ramiasa *et al.* 2014). The CL dynamics is known to be extremely sensitive to the physical roughness and/or chemical heterogeneity on the solid surface, which cause the dynamic contact angle θ between the liquid and solid surfaces to depend on the direction of fluid motion (Leger & Joannyde 1992), with the advancing contact angle θ_a being larger than the receding angle θ_r.

The dynamics of spreading of a wetting liquid on an ambient solid surface is a relaxation process for the liquid interface to reach its equilibrium shape. In addition to the difficulty

involved in the solution of a moving CL at the edge of the advancing liquid, the behavior
of the liquid in the vicinity of the CL presents further complications. The hydrodynamic
friction coefficient ξ_{in} in the wedge-shaped region away from the CL has the form (de
Gennes *et al.* 2004)

$$\xi_{in} \simeq \frac{3\ln\varepsilon}{\theta}\pi d\eta \equiv \alpha_{in}\pi d\eta, \qquad (1.1)$$

for liquids with a small contact angle θ. In the above, πd is the contact line length, η is
the fluid viscosity, and $\varepsilon \simeq R/a$ is a cut-off parameter with R being a macroscopic size
of the system and a (~ 1 nm) being a microscopic cut-off length to avoid the dissipation
divergence of the moving CL. The value of α_{in} in Eq. (1.1) is $\alpha_{in} \simeq 27.6/\theta$ (for $\varepsilon \simeq 10^4$),
which is very large for liquids with small θ and even becomes divergent when $\theta \to 0$.

For liquid drops of radius R smaller than the capillary length $\lambda_c = (\gamma/\rho g)^{1/2}$, which is
a measure of importance of the liquid-air interfacial tension γ relative to the gravitational
force ρg, the effect of gravity can be ignored and liquid spreading is driven primarily by
the imbalanced interfacial force per unit length normal to the CL,

$$F_d = \gamma\left(\cos\theta - \cos\theta_{eq}\right) \simeq \frac{\gamma}{2}\theta^2. \qquad (1.2)$$

The last equality in Eq. (1.2) is obtained by assuming that the dynamic contact angle θ is
small and equilibrium contact angle $\theta_{eq} = 0$. For a water-air interface with $\gamma \simeq 73\ mN/m$,
liquid density $\rho = 10^3\ kg/m^3$, and gravitational acceleration $g = 9.8\ m/s^2$, we have
$\lambda_c \simeq 2.7\ mm$. In the simple case when the solid surface is smooth and homogeneous so
that CL pinning can be ignored, the approach to equilibrium is determined by a balance
between the capillary force given in Eq. (1.2) and viscous dissipation given in Eq. (1.1).
This force balance gives rise to a power-law relaxation as manifested by Tanner's law,
$R(t) \sim t^m$, for the viscous spreading of small liquid drops of radius $R(t)$ as a function of
time t (Tanner 1979; de Gennes *et al.* 2004). The power-law exponent $m = 1/10$ was
observed in various spreading experiments (Bonn *et al.* 2013).

For many ambient solid surfaces of interest, however, they are not homogeneous and the
motion of a CL is often pinned by the physical roughness and/or chemical inhomogeneity
on the solid surface. As a result, the relaxation of the liquid interface to its equilibrium
shape is no longer determined by the viscous dissipation near the edge of the advanc-
ing liquid (Pagonabarraga 2012). Instead, the relaxation is accomplished by activated
hopping of the CL over a complex potential landscape generated by nano-scale surface
heterogeneities (Kaz *et al.* 2012; Guan *et al.*, 2016a,b). In this case, the CL was found
to relax logarithmically in time t [i.e., go as $\ln(\Gamma t)$] at the long-time limit. The relaxation
rate Γ is determined by the barrier crossing dynamics with $\Gamma \sim k_0 \exp(-E_b/k_B T)$, where
E_b is the energy barrier height, $k_B T$ is the thermal energy of the system, and k_0 is a
typical attempt frequency.

In this paper, we consider a different scenario of the CL relaxation, which also leads to
a logarithmic aging of the CL. As shown in Fig. 1(a), when a thin glass fiber of diameter
d ($\sim 2\ \mu$m) intersects a free-standing soap film, the liquid (water) in the soap film wets
the fiber surface and two soap film menisci develop with two advancing CLs moving in
the opposite directions along the fiber. When the film thickness $\ell > d$ (thick film limit),
the fluid flow toward the fiber is not confined very much by the soap film so that the film
meniscus can develop quickly. It was shown by Clanet & Quéré (2002) that the rising
time for a liquid-air interface to creep along a vertical fiber and reach its equilibrium
shape scales as Γ_0^{-1} with $\Gamma_0 = \gamma/[\eta(d/2)]$ being the interface relaxation rate. Because
the capillary speed γ/η is very fast (~ 23 m/s for an interface with $\gamma = 23\ mN/m$ and
$\eta = 1\ cP$), it only takes a few microseconds for the interface to reach its equilibrium
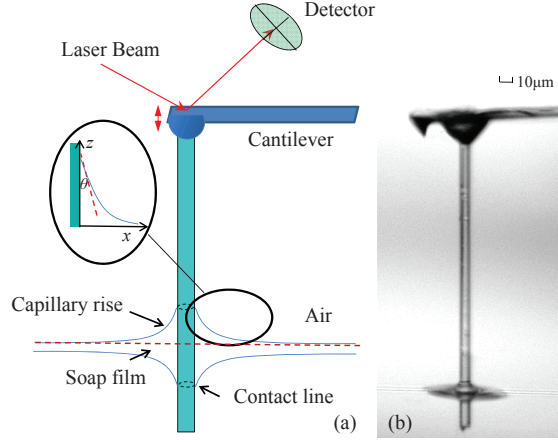
FIGURE 1. (a) Sketch of the AFM-based hanging fiber probe intersecting a thin soap film. The dashed circles on the fiber surface show the two contact lines formed on each side of the soap film. Inset shows the geometry near the contact line and the coordinate system used in the experiment. (b) A microscope picture of a glass fiber of diameter $d = 8 \ \mu m$ and length $\sim 300 \ \mu m$ intersecting a thin soap film.

shape (de Gennes *et al.* 2004)

$$\frac{x(z) + d/2}{b} = \cosh\left[\frac{z}{b} - \ln\left(\frac{2\lambda_c}{b}\right)\right], \tag{1.3}$$

where z is the meniscus height, x is its radial location, and $b = (d/2)\cos\theta_{eq}$. Here we use a coordinate system with $x = 0$ at the fiber surface and $z = 0$ at the unperturbed liquid-air interface, as shown in the inset of Fig. 1(a).

Equation (1.3) was obtained by assuming the liquid interface is stationary so that the two principle curvatures of the meniscus cancel out with each other, leading to a zero Laplace pressure at any point of the meniscus. The capillary length λ_c is used to set the cut-off length of the horizontal extent of the meniscus. The height of capillary rise, $h_{eq} \equiv z(x = 0)$, on the fiber surface can be obtained by inverting Eq. (1.3) (Wang *et al.*, 2016)

$$h_{eq} = \frac{d\cos\theta_{eq}}{2}\ln\left[\frac{4\lambda_c}{d(1 + \sin\theta_{eq})}\right]. \tag{1.4}$$

At this meniscus height, the capillary force is balanced by the weight of the wetting liquid and the interface reaches equilibrium.

When the film thickness $\ell < d$ (thin film limit), the fluid flow in the soap film is found to be strongly confined by the soap film thickness. As a result, the film meniscus creeps slowly along the vertical fiber and reaches its equilibrium height logarithmically in time t (at the long-time limit). It is shown that the relaxation rate Γ in this case is determined by the viscous dissipation in the bulk region of the soap film with $\Gamma \simeq \Gamma_0[\ell/(d/2)]^2$. In the experiment, we find that the confinement factor $[\ell/(d/2)]^2$ can be as small as 10^{-4}. The main aim of this work is twofold. First, we conduct systematic measurements of the height of capillary rise $h(t)$ along the glass fiber and the viscous friction coefficient $\xi(t)$ felt by the glass fiber in contact with a soap film, both as a function of fiber draining time t. Second, we present a new theoretical approach based on the Onsager variational principle (Doi 2011, 2013), which is used to describe the dynamics of spreading of a thin soap film along the glass fiber. The newly derived equations of motion provide the

FIGURE 2. A metal ring of diameter 1 cm is used to support a soap film.

analytical solutions of the height of capillary rise $h(t)$ and contact angle $\theta(t)$, which are found to be in good agreement with the experimental results. Our work thus provides a common framework for understanding the confinement effect of thin soap films in the dynamics of spreading along a fiber.

The remainder of the paper is organized as follows. We first describe the experimental methods in § 2. Experimental results are presented in § 3. Further theoretical analysis is given in § 4. Finally, the work is summarized in § 5.

2. Experiment

2.1. *Preparation of soap films*

The experimental apparatus and procedures used in this experiment are similar to those described previously (Guo *et al.,* 2015), and here we only mention some key points. The soap solution is prepared by mixing a commercial detergent (Ultra Joy dishwashing liquid) with a solution of glycerine and deionized water of resistivity 18 MΩ·cm (purified by a Barnstead three-column e-pure system). For all the solutions used in the experiment, the concentration of the detergent is kept at 1 wt.%. The viscosity η of the soap solution thus depends only on the amount of glycerine in the aqueous solution and is not affected much by the detergent. By varying the mass concentration of glycerine from 20 to 65 wt.%, the viscosity η of the soap solution changes from 1.65 to 13.7 cP.

A glass pipette containing the soap solution is used to blow soap bubbles, which are then transferred to a supporting substrate for optical imaging and AFM measurement. A metal ring of diameter 1 cm is used to support the soap film, as shown in Fig. 2. The liquid in the soap film drains very slowly along the metal ring to a plastic container on the bottom (not shown). It is found that the initial value of the soap film thickness ℓ can vary from micrometers to tens of nanometers, depending on the film viscosity η. Soap films with a higher viscosity tend to be thicker initially.

The film thickness ℓ is measured using a UV-visible spectrophotometer (Perkin Elmer, Lambda 20), following a standard procedure (Huibers & Shah 1997). When a laser beam passes through a transparent film, the amplitude of the transmitted light is determined by the interference effect between the reflected beams from the two film-air interfaces. From the measured transmission spectrum, one can determine the film thickness ℓ. The minimum value of ℓ measurable by this spectrophotometer is 35 nm. Typically, the soap film can last for about an hour before it bursts. At the final stage of draining, the soap film becomes a Newton black film with a thickness of several nanometers (Poulin *et al.,* 1996). To speed up the draining process, one may use a filter paper to touch the soap
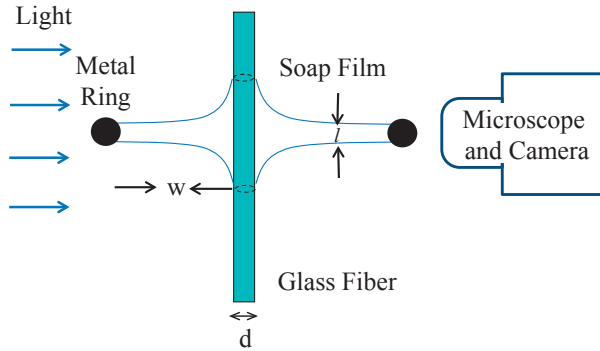
FIGURE 3. Side view of the optical imaging setup. The two black solid circles indicate the metal ring used to support the soap film. The radius of the soap film is w ($\simeq 0.5$ cm) and its thickness is ℓ. The vertical glass fiber intersecting the soap film has a diameter d in the range of 4-20 μm. The dashed circles on the surface of the glass fiber show the two contact lines formed on each side of the soap film.

film for 4-5 s and soak the liquid away. A soap film with $\ell \lesssim 100$ nm can be prepared in this way without much waiting time. Previously, we measured the film thickness ℓ at different draining times using the spectrophotometer (Guo *et al.*, 2015). With the same procedure, we measure the time-dependence of ℓ in this experiment and use it as a guideline to estimate the initial value of the film thickness ℓ.

2.2. *Optical imaging of soap film meniscus along a fiber*

Figure 3 shows a homemade optical imaging setup for the study of temporal evolution of soap film meniscus along a thin glass fiber. An LCD light source (Schott KL2500) is used for bright field illumination. A plasma-cleaned glass fiber of diameter d in the range of 4-20 μm is held vertically with a three-dimensional micromanipulator and pierces through the soap film with a penetration tip (~ 40 μm) below the soap film. This penetration tip is long enough for the soap film meniscus to develop on each side of the soap film. A pinhole of 2 mm in diameter is placed between the light source and the film meniscus to collimate the light beam and allow a clear observation of the film meniscus under a stereo-microscope (Leica MZ16 with $\times 57.5$ magnification). The images of a growing film meniscus are recorded by a CCD camera (Photometrics CoolSNAP EZ) with a spatial resolution 1392$\times$1040. The movie recording of the microscope images is typically taken at the sampling rate of 0.5 frames per second (fps) and is controlled by the μManager software.

2.3. *Operation of the "long needle" atomic force microscope*

In the experiment, we use a recently developed hanging fiber probe (Xiong *et al.* 2009; Guo *et al.*, 2014) based on atomic force microscopy (AFM) to measure the change of the friction coefficient $\xi(t)$, when a soap film creeps along the hanging fiber probe. As shown in Fig. 1(b), the "long needle" AFM consists of a vertical glass fiber of diameter d in the range of 0.4-4 μm and length 100-300 μm, which is glued onto the front end of a rectangular cantilever beam. The AFM cantilever is mounted on a piezoelectric tube scanner to provide vertical motion with accuracy down to nanometers. The other end of the fiber is in contact with the soap film. The intersection between the soap film and the fiber surface forms two circular contact lines, as shown by the two dashed lines in

Fig. 1(a). The assembly and calibration of the hanging fiber probe have been described elsewhere (Xiong *et al.* 2009; Guo *et al.,* 2014).

The hanging fiber probe can measure two important properties of the CL. First, it acts as an accurate force sensor capable of measuring the capillary force (Wang *et al.,* 2016; Guan *et al.,* 2016a,b),

$$f = -\pi d\gamma \cos\theta, \tag{2.1}$$

acting on the CL of length πd, which is formed on the fiber surface with a *single* liquid interface of surface tension γ and contact angle θ. Here the sign of f is defined as $f \leq 0$ for $\theta \leq 90°$ and $f > 0$ for $\theta > 90°$. With an accurate calibration of the cantilever, the AFM can measure the capillary force down to $\sim$10 pN at the accuracy of 0.2%.

Second, the hanging fiber probe can be used as a high-quality mechanical resonator, which oscillates vertically (along the z-axis) with a resonant frequency $\omega_0 = (k/m)^{1/2}$ ($\sim$600 kHz), where m is the effective mass of the modified cantilever and k is its spring constant. Being operated at a resonant state, the hanging fiber amplifies the fluctuation spectrum and thus can accurately detect minute changes of the friction coefficient $\xi(t)$ caused by the viscous damping in the soap film. The quantity measured in the experiment is the power spectrum of the vertical deflections of the cantilever, $|z(\omega)|^2$, which has an analytical form (Ma *et al.* 2000; Xiong *et al.* 2009)

$$|z(\omega)|^2 = \frac{2k_B T\xi/m^2}{(\omega^2 - \omega_0^2)^2 + (\omega\xi/m)^2}, \tag{2.2}$$

where $\omega = 2\pi f$ is the angular frequency. By fitting the measured $|z(\omega)|^2$ (or $|z(f)|^2$) to Eq. (2.2), one obtains the fitted values of k, m and ξ.

Measurements of $|z(f)|^2$ are conducted using an AFM (MFP-3D, Asylum Research Inc.) operated under the thermal power spectral density (PSD) mode. Typically, $|z(f)|^2$ is taken with a frequency resolution of 152 Hz and the averaging time for each $|z(f)|^2$ is set for approximately 1 min. To determine the absolute value of $|z(f)|^2$, the output voltage signal from the position-sensitive detector is calibrated against known values of the cantilever deflection. The experimental uncertainties of the measured $|z(f)|^2$ can be kept at the level of 5-10%. The hanging fiber probe has been thoroughly tested in previous experiments and more experimental details about how to obtain the value of ξ at the liquid-air interfaces have been reported elsewhere (Guo *et al.,* 2013, 2014). More recently, this technique was used to measure the friction coefficient ξ_c of a fluctuating CL at equilibrium for a soap film (Guo *et al.,* 2015).

2.4. *AFM measurements of the soap film thickness ℓ and the height of capillary rise h*

Figure 4(a) shows a typical evolution curve of the measured capillary force f, when the hanging fiber probe pierces through a soap film. The black curve ($\rightarrow$) shows how the measured f changes when the glass fiber is pushed downward at a constant speed $U = 10\ \mu m/s$. Once the fiber tip touches the upper surface of the soap film at $Z \simeq 12.3\ \mu m$, a capillary force, $f \simeq -125.4\ nN$, is detected. The minus sign indicates that the capillary force pulls down the fiber ($\theta < 90°$). In a previous experiment (Guo *et al.,* 2015), we found that when the soap film is thick enough ($\ell \geq 1.6\ \mu m$), the measured f can reach a plateau value before the fiber tip touches the lower surface of the soap film. This plateau value of f agrees well with that obtained when the hanging fiber was in contact with a single liquid-air interface of the soap solution, of which the soap film is made. From the measured capillary force [see Eq. (2.1)], we found the contact angle $\theta \simeq 0°$ and surface tension $\gamma = 23.2\ mN/m$ for all the soap solutions used on a clean glass fiber. In Fig. 4(a), however, no plateau region is observed for the measured f in the advancing direction and
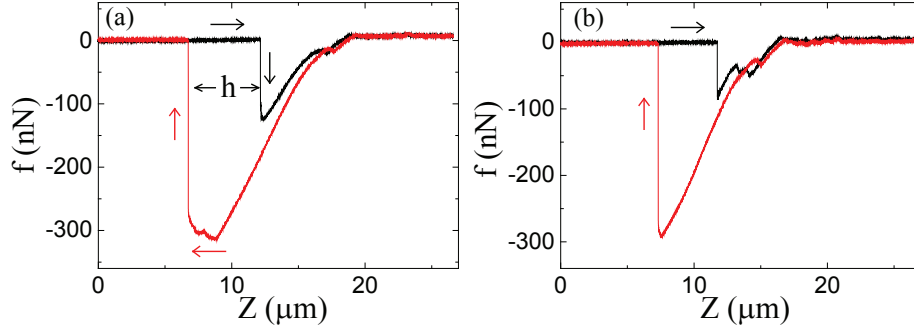
FIGURE 4. Variations of the measured capillary force f when a glass fiber pierces through (a) a thick soap film with thickness $\ell \sim 1~\mu m$ and (b) a thinner soap film with $\ell < 35$ nm. The black curves ($\rightarrow$) show how the measured f changes when the glass fiber is pushed downward at a constant speed $U = 10~\mu$m/s. The red curves ($\leftarrow$) show how the measured f changes when the glass fiber is pulled upward at the same speed.

only a short transient of f is observed when the fiber tip pierces through the entire soap film. We therefore conclude that the film thickness in this case is smaller than 1.6 μm.

When the fiber tip touches the lower surface of the soap film at $Z \simeq 12.3~\mu m$, another CL forms on the fiber surface with an initial contact angle $\theta_l = 90°$. Now the total force acting on the fiber is, $f = \pi d\gamma(1 - \cos\theta_l)$, which is a sum of two capillary forces of opposite signs. As the fiber further moves downward, the value of θ_l decreases and reaches its equilibrium value, $\theta_l \simeq 0°$, at $Z \simeq 18.9~\mu m$. Thus the total force is canceled out and we have $f = 0$. This is shown in Fig. 4(a) for $Z \geq 18.9~\mu m$. In this case, the fiber is under zero external force, as if it is in air.

The red curve ($\leftarrow$) in Fig. 4(a) shows how the measured f changes when the glass fiber is pulled back upward at the same speed U. The value of f starts to decrease from zero when the fiber tip retracts back to the lower surface of the soap film at $Z \simeq 18.9~\mu m$. As the fiber further moves upward, the contact angle θ_l of the lower capillary rise changes continuously from 0° to 90° and finally the lower surface snaps off from the fiber tip. The maximum force measured is $f = \pi d\gamma$ when only the upper surface of the soap film is in contact with the fiber at the contact angle $\theta \simeq 0°$. Before the fiber tip detaches from the soap film, the capillary force increases slightly and then drops quickly to zero. This round-off feature was also observed for a single liquid-air interface (Yazdanpanah *et al.,* 2008), indicating that the thick soap film used to obtain Fig. 4(a) shares some common properties of the liquid-air interface. The round-off feature is absent for a thin film as shown in Fig. 4(b). The distance h ($\simeq 5.4~\mu m$) between the black and red vertical lines in Fig. 4(a) gives the height of capillary rise of the soap film meniscus on the fiber surface. As will be shown below, the actual value of h changes with the fiber draining time after the fiber touches the soap film.

When the film thickness $\ell << 1~\mu m$, as shown in Fig. 4(b), the transient region of the measured f in the advancing direction becomes even shorter. In this case, one can still get a good estimate of the height of capillary rise h. While the capillary force measurements shown in Fig. 4 cannot provide an accurate real-time measurement of ℓ, they nevertheless can tell us whether the soap film is in the thick film regime ($\ell \sim 1~\mu m$) or in the thin film regime ($\ell \sim 10~nm$).
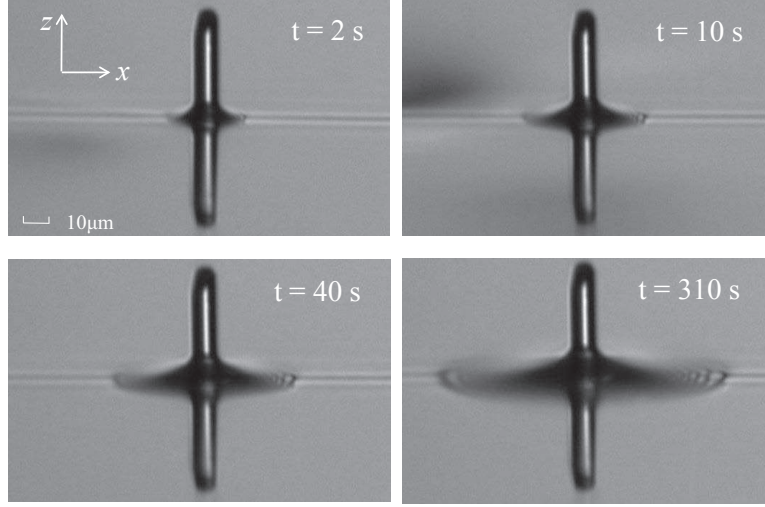
FIGURE 5. Microscope images of the soap film meniscus in the vicinity of a vertical glass fiber of diameter $d = 9$ μm. The images are taken at different times after the fiber tip pierces through the soap film from below ($t = 0$). The glass fiber is kept stationary intersecting the soap film during the entire movie taking. The measurements are made for a soap film with viscosity η = 1.65 cP and its thickness is estimated to be $\ell \sim 100$ nm. The scale bar for all the images is 10 μm.

3. Experimental Results

3.1. *Temporal evolution of soap film meniscus along a fiber*

Figure 5 shows how the soap film meniscus in the vicinity of a vertical glass fiber evolves after the fiber tip pierces through the soap film from below ($t = 0$). Hereafter, we refer to this time as the fiber draining time t. The movie recording is typically taken at the sampling rate of 0.5 fps, and here we only show some representative images at different fiber draining times. The thin horizontal line in the middle of the image shows the film-air interface. The portion of the fiber above the interface is the penetration tip. Below the interface, there is a reflection image of the penetration tip by the soap film. Two capillary rises form around the fiber surface and they are symmetrically aligned on the two sides of the soap film, so that the resulting capillary force acting on the fiber is zero when the two capillary rises are fully developed (see Fig. 4). The two capillary rises change the reflection of light, forming a dark region surrounding the fiber as observed under a microscope. It is seen from Fig. 5 that this dark region grows with the fiber draining time t, indicating that the soap film meniscus in the vicinity of the vertical fiber rises slowly with t. This meniscus growth is accomplished by an inward-going flow within the soap film toward the fiber, which then creeps along the vertical fiber in both directions.

It is found that such a creeping flow depends sensitively on the film thickness ℓ. When $\ell \gtrsim d$, a fully developed capillary rise forms almost immediately (< 1 s) and no visible change is observed for the soap film during the experimental time (1-200 s). The creeping speed of the capillary rise in this thick-film regime is expected to be the same as that for a single liquid-air interface. When the film thickness is reduced to the range 10 $nm \lesssim \ell \lesssim d$, we observe the time-dependence of the capillary rise formation, as shown in Fig. 5. The meniscus growth rate in this intermediate regime is so slow that one can record the dynamics at a sampling rate of 0.5 fps. When the film thickness is further reduced to the range $\ell \lesssim 10$ nm, the soap film becomes a Newton black film (Poulin *et al.,* 1996). In this

t = 0 s   t = 60 s   t = 120 s   t = 189 s
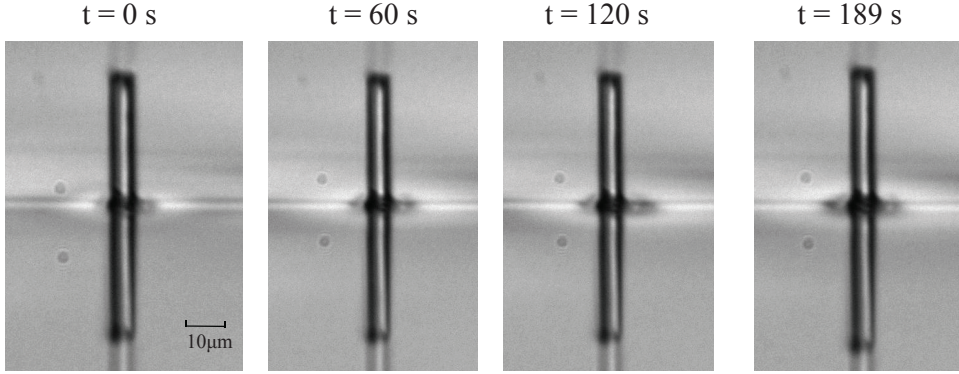

FIGURE 6. Microscope images of the soap film meniscus in the vicinity of a vertical glass fiber of diameter $d = 6$ μm. The images are taken at different times after the fiber tip pierces through the soap film from below ($t = 0$). The glass fiber is kept stationary intersecting the soap film during the entire movie taking. The measurements are made for a soap film with viscosity $\eta = 1.65$ cP and its thickness is estimated to be $\ell < 10$ nm (Newton black film). The scale bar for all the images is 10 μm.
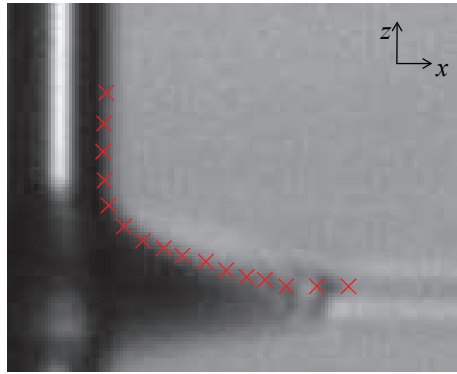

FIGURE 7. Magnified image of the soap film meniscus near a vertical glass fiber at $t = 10$ s. Red crosses show the meniscus profile of the soap film, which is detected by the edge of the contrast difference in the image. The horizontal line at the lower-right corner in connection with the red crosses is the undisturbed film-air interface. Also shown is the coordinate system used for the image analysis of the meniscus profile (see text for more details).

case, the volume of liquid in the capillary rise region is small and does not change much during the experimental time ($t < 200$ s). Figure 6 shows a time lapse of the soap film meniscus at this thin-film limit with $\ell \lesssim 10$ nm. No visible change is observed among the microscope images taken at different fiber training times.

   The captured images as shown in Fig. 5 are further analyzed to locate the edge of the contrast difference using the ImageJ software, from which we obtain the profile of the soap film meniscus near the glass fiber. Figure 7 shows an example, in which the red crosses are used to mark the meniscus profile. In the image analysis, the meniscus profile is extended both vertically along the $+z$ direction to include part of the glass fiber and horizontally along the $+x$ direction to include part of the unperturbed film-air interface. The typical error in determining the soap film meniscus is about 1 pixel ($\simeq 0.24$ μm).

   Figure 8(a) shows an example of the resulting meniscus profile $z(x, t)$ of the soap film as a function of distance x away from the fiber surface. In the plot, both the vertical axis z and horizontal axis x are normalized by the fiber diameter d ($= 9$ μm). It is found that
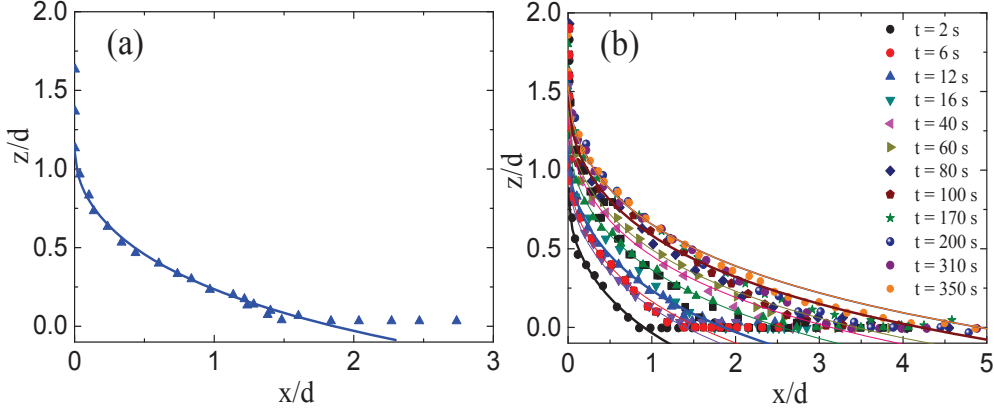
FIGURE 8. (a) Obtained meniscus profile $z(x, t)$ as a function of distance x away from the fiber surface at $t = 12$ s. The numerical data of the meniscus profile are obtained from the image analysis as shown in Fig. 7. Both the z- and x- axes are normalized by the fiber diameter d ($= 9\ \mu m$). The solid line shows a fit of Eq. (3.1) to the data points with two fitting parameters: the height of capillary rise $h = 1.12d$ and contact angle $\theta = 0°$. (b) Variations of the meniscus profile $z(x, t)$ at different fiber draining times from $t = 2$ s to $t = 350$ s. The solid lines show the fits of Eq. (3.1) to different sets of data with $h(t)$ and $\theta(t)$ as two fitting parameters.

at a given fiber draining time t, the obtained $z(x, t)$ has a similar functional form as the equilibrium profile given in Eq. (1.3) but with two time-dependent parameters $h(t)$ and $b(t)$. To show this more clearly, we invert the equation $(x + d/2)/b = \cosh([z - h]/b)$ and write the final equation as

$$\frac{z(x, t)}{b} = \frac{h(t)}{b} - \ln\left(\frac{x + d/2}{b} + \left[\left(\frac{x + d/2}{b}\right)^2 - 1\right]^{1/2}\right), \qquad (3.1)$$

where $h(t)$ is the height of capillary rise on the fiber surface and $b(t) = (d/2)\cos\theta(t)$. To get Eq. (3.1), we chose a solution in which the boundary condition $z = 0$ at large values of x is satisfied. When the two time-dependent parameters, $h(t)$ and $\theta(t)$, reach their equilibrium values h_{eq} and θ_{eq}, respectively, $z(x, t)$ in Eq. (3.1) becomes the equilibrium profile. The solid line shows a fit of Eq. (3.1) to the data points with $h(t)$ and $\theta(t)$ as two fitting parameters. As mentioned above, the image analysis of the meniscus profile included a part of the fiber surface along the vertical $+z$ direction and a part of the unperturbed film-air interface along the horizontal $+x$ direction. Therefore, both ends of the meniscus profile are not included in the fitting. It is seen that the measured $z(x, t)$ is well described by Eq. (3.1) at a fixed time t.

Figure 8(b) shows how the meniscus profile $z(x, t)$ evolves with the fiber draining time t. It is seen that as t increases, the soap film creeps along the vertical glass fiber with both the height and volume of the capillary rise increasing slowly with t. All of the meniscus profiles at different draining times are found to be well described by Eq. (3.1) (solid lines), indicating that the soap film meniscus is in a quasi-equilibrium state at any given time. This is because the creeping flow is slow compared with the "instantaneous" change of the meniscus shape, which is determined by the balance of local Laplace pressure. There are two time-dependent fitting parameters in Eq. (3.1). It is found that all of the meniscus profiles can be fit with a common contact angle $\theta = 0° \pm 20°$. The fitted value of θ agrees with that obtained from the direct AFM measurement of the capillary force, as discussed in Sec. 2.4. It has a relatively larger error, because $\cos\theta$ in Eq. (3.1) is not
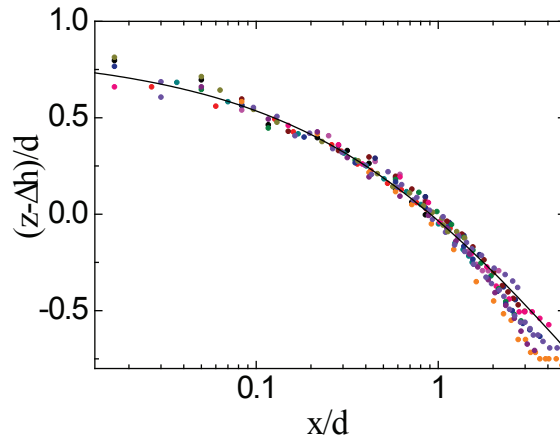
FIGURE 9. Scaling plot of the measured meniscus profile, $z(x,t) - \Delta h(t)$, as a function of distance x away from the fiber surface. Both the vertical and horizontal axes are normalized by the fiber diameter d ($= 9\ \mu m$). Black circles show the unshifted meniscus profile with $\Delta h = 0$ at $t_0 = 2\ s$. The solid line shows a fit of Eq. (3.1) to all the data points with $\theta = 0°$ and $h(t) = h_0 = 0.85d$. The color code used for other sets of data is the same as that used in Fig. 8.

very sensitive to small changes of θ when θ is close to zero. The temporal evolution of the soap film meniscus is then uniquely determined by Eq. (3.1) with the time-varying height of capillary rise $h(t)$ as the only fitting parameter. The initial value of $h(t)$ is $h_0 \simeq 0.85d$ at $t_0 = 2\ s$, which is the earliest time at which we can measure the meniscus profile. As mentioned above, the change of $h(t)$ with t is spontaneous as the soap film slowly creeps along the glass fiber.

As shown in Eq. (3.1), $h(t)$ is simply an offset value of z when $x = 0$. To determine the value of $h(t)$ more accurately, we vertically shift the meniscus profiles $z(x,t)$ obtained at different t by an amount $\Delta h(t)$, so that all of the measured meniscus profiles overlap with that obtained at $t_0 = 2\ s$, which is not shifted ($\Delta h = 0$). Indeed, after the subtraction of the vertical shift $\Delta h(t)$, all of the data sets collapse on to a master curve, as shown in Fig. 9. In the plot, those data points on the fiber surface with $x = 0$ and those at the undisturbed soap film interface with $z = 0$ are not included. The solid line shows a fit of Eq. (3.1) to all the data points with $\theta = 0°$ and $h(t) = h_0 = 0.85d$. Figure 9 thus demonstrates that the meniscus profile $z(x,t)$ of the soap film at any given time t can indeed be described by a quasi-equilibrium shape with zero curvature as shown in Eq. (3.1). This is attributed to the slowness of the film evolution. The time-dependence of $h(t)$ is then accurately determined by

$$h(t) = h_0 + \Delta h(t), \tag{3.2}$$

where h_0 is the value of $h(t)$ at the initial time t_0. For the soap film shown in Fig. 9, we find $h_0 = 0.85d$.

Figure 10 shows how the measured $h(t)$ varies with t. Two sets of data with different values of ℓ and d are presented. The black circles are obtained for a soap film with thickness $\ell \sim 100\ nm$, and the red triangles are obtained for a soap film with thickness $\ell \sim 50\ nm$. It is seen that the measured $h(t)$ is a monotonically increasing function of t from its initial value h_0 to its final value. The initial height h_0 is found to increase with the film thickness ℓ. This finding confirms that the slow evolution of $h(t)$ is caused by the confinement of the creeping flow inside the thin soap film; the higher the degree of confinement is, the slower the meniscus profile evolves.
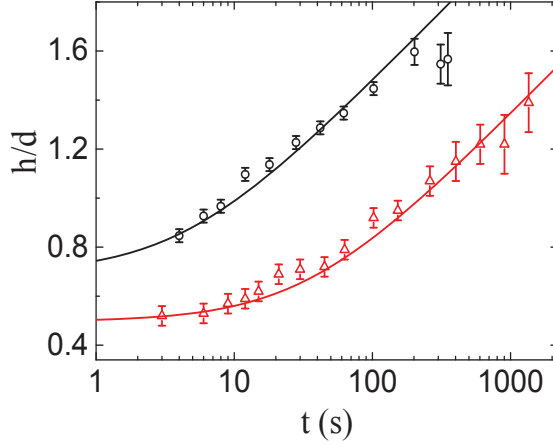
FIGURE 10. Obtained height of capillary rise $h(t)$ as a function of fiber draining time t for two soap film systems. The black circles are obtained for a soap film with thickness $\ell \sim 100$ nm and fiber diameter $d = 9$ μm. The red triangles are obtained for a soap film with thickness $\ell \sim 50$ nm and fiber diameter $d = 6$ μm. In the plot, $h(t)$ is normalized by the fiber diameter d. The error bars show the experimental uncertainty of the measurements. The solid lines show the fits of Eq. (4.23) to the two sets of data with $c_0 = 4.0$ and $\Gamma = 0.9$ for the black curve and $c_0 = 1.8$ and $\Gamma = 0.05$ for the red curve.

As shown in Fig. 5, the image contrast of the soap film meniscus decreases with increasing t (see, e.g., the $t = 310$ s panel), which causes deviations of the measured meniscus profile $z(x,t)$ from the expected quasi-equilibrium shape given in Eq. (3.1). These deviations are visible in Fig. 8(b) for the curve fitting to the orange circles at $t = 350$ s and also in Fig. 9. Consequently, the obtained values of $h(t)$ at the late stage suffer relatively larger errors. While the experimental uncertainties could be reduced by further improvement in the collimation of light illumination and reduction of scattered light from the liquid interface, the two data sets shown in Fig. 10, nevertheless, show a smooth and continuous increase over a time span of almost three decades.

At the very late stage, the soap film meniscus is expected to reach its equilibrium height h_{eq}, like a bulk liquid does. The value of h_{eq} is given in Eq. (1.4). For a soap film system with surface tension $\gamma = 23.2$ mN/m, liquid density $\rho = 10^3$ kg/m^3, contact angle $\theta = 0°$ and $d = 5$ μm, we find $h_{eq} \simeq 3.6d$. Clearly, the two sets of data shown in Fig. 10 have not reached their asymptotic height yet.

3.2. *Temporal evolution of fiber dissipation*

To further study the development of the meniscus profile of soap films along a thin fiber, we use the "long needle" AFM to measure the power spectrum $|z(f)|^2$ for soap films at different fiber draining times t. Figure 11 shows how the measured $|z(f)|^2$ changes with t. In the measurement, the hanging fiber is kept still after it pierces through a soap film. It is found that the resonant peak changes continuously with increasing t; the frequency peak broadens while the peak height decreases and peak position shifts to lower frequencies. Figure 11 shows the changes of the measured $|z(f)|^2$ at two representative draining times. The measured $|z(f)|^2$ is well described by Eq. (2.2) (solid lines) with spring constant k, mass m and friction coefficient ξ as three fitting parameters. It is found that the fitted values of k and m remain approximately constant for different draining times but the fitted value of ξ changes sensitively with t. From the measured $|z(f)|^2$ at different t, we
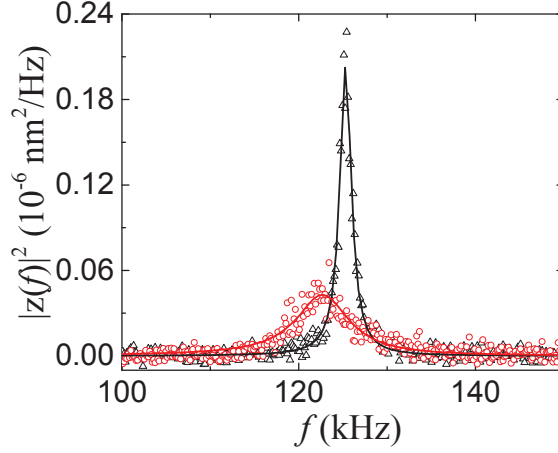
FIGURE 11. Variations of the measured power spectrum $|z(f)|^2$ for a soap film at two different fiber draining times: $t = 120\ s$ (black triangles) and $t = 2520\ s$ (red circles). The measurements are made when the hanging fiber probe of diameter $d = 2.6\ \mu m$ is kept stationary intersecting the soap film of viscosity $\eta = 1.65\ cP$ and thickness $\ell \sim 50\ nm$. The solid lines show the fits of Eq. (2.2) to the two sets of data with the fitting parameters, $\xi = 2.75 \times 10^{-7}$ Ns/m, $k = 31.62$ N/m and $m = 5.10 \times 10^{-8}$ g for the black triangles and $\xi = 2.97 \times 10^{-6}$ Ns/m, $k = 31.57$ N/m and $m = 5.26 \times 10^{-8}$ g for the red circles.

obtain $\xi(t)$ as a function of t. Similarly, we also measure $|z(f)|^2$ when the fiber is in air and obtain the corresponding friction coefficient ξ_a, which is independent of t.

By integrating Eq. (2.2), one finds that the mean-square value of soap film fluctuations is given by the equipartition theorem, $k\langle z^2(t)\rangle_t = k_B T$. For $k = 31.6\ N/m$, we have $\langle z^2(t)\rangle_t^{1/2} \simeq 1.14 \times 10^{-2}\ nm$. The corresponding drag force is $f_d \simeq \xi\omega_0\langle z^2(t)\rangle_t^{1/2} \simeq 26.2\ pN$ and the capillary number $Ca \simeq \eta\omega_0\langle z^2(t)\rangle_t^{1/2}/\gamma \simeq 6.27 \times 10^{-7}$ for the soap film with $\gamma = 23.2$ mN/m, $\xi = 2.97 \times 10^{-6}$ Ns/m, $\omega_0 = 2\pi\times123$ kHz, and η=1.65 cP. These numbers reveal the tremendous sensitivity of the technique useful for the study of soap film dissipation.

Figure 12 shows the obtained net friction coefficient $\Delta\xi(t) \equiv \xi(t) - \xi_a$ as a function of t for five samples with different values of d and η. All the data sets reveal a general trend that the obtained $\Delta\xi(t)$ increases with t for more than two decades of time span. It is found that the rate of increase of $\Delta\xi(t)$ depends sensitively on the film thickness ℓ. For thick films with $\ell \sim 1\ \mu m$ (red triangles and red circles), their rate of increase is much faster than that of thinner films with $\ell \sim 100\ nm$ (black and green triangles and blue diamonds). Here we estimate the value of ℓ based on the AFM force-curve measurements as shown in Fig. 4.

In a previous experiment (Guo *et al.,* 2015), it was found that the net friction coefficient $\Delta\xi(t)$ contains two contributions:

$$\Delta\xi(t) = \xi_c + \xi_s(t). \qquad (3.3)$$

The first term ξ_c is the contribution from the two (fluctuating) CLs, which is independent of t. The measured ξ_c in the thin film limit ($\ell \sim 10\ nm$) was found to have a scaling form (Guo *et al.,* 2015),

$$\xi_c = 2\alpha\pi d\eta, \qquad (3.4)$$

where $\alpha = 1.1 \pm 0.3$ is a numerical coefficient independent of the contact angle θ. The factor of 2 accounts for the two CLs formed on the fiber surface. The second term $\xi_s(t)$
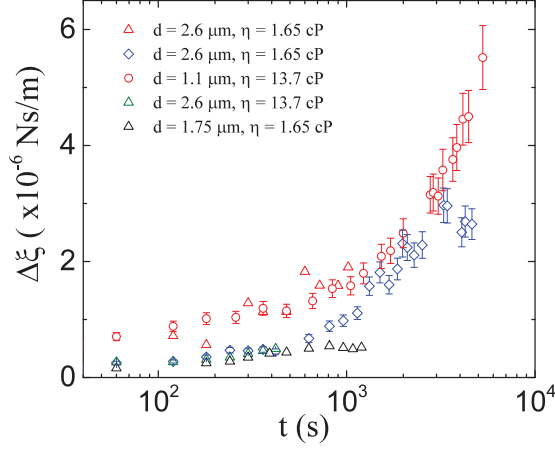
FIGURE 12. Obtained net friction coefficient $\Delta\xi(t)$ as a function of fiber draining time t for five samples with different fiber diameters d and soap film viscosities η: $d = 2.6 \ \mu m$ and $\eta = 1.65 \ cP$ (red triangles); $d = 2.6 \ \mu m$ and $\eta = 1.65 \ cP$ (blue diamonds); $d = 1.1 \ \mu m$ and $\eta = 13.7 \ cP$ (red circles); $d = 2.6 \ \mu m$ and $\eta = 13.7 \ cP$ (green triangles); $d = 1.75 \ \mu m$ and $\eta = 1.65 \ cP$ (black triangles). The film thickness ℓ of the five samples is discussed in the text.

in Eq. (3.3) is the sidewall contribution from the fluid in contact with the hanging fiber. As the soap film creeps along the vertical fiber, $h(t)$ increases and so does the contact area between the fluid and fiber. As a result, $\xi_s(t)$ increases with $h(t)$. This explains the observed time-dependence of the measured $\Delta\xi(t)$ in Fig. 12 and the faster increase of $\Delta\xi(t)$ associated with the thicker films. It is also found that for sufficiently large values of t, $\xi_s(t)$ becomes the dominant term in the measured $\Delta\xi(t)$.

4. Theoretical analysis

The above experimental results suggest that the slow creeping flow along the vertical glass fiber is driven by the capillary force between the soap film and fiber surface. This creeping flow is strongly influenced by the confinement effects on viscous dissipation in the thin soap film. With these observations, we now carry out a theoretical analysis of the scaling properties of the creeping flow.

4.1. *The Onsager principle applied to capillary rise*

The flow inside the soap film is in the Stokesian regime, as its Reynolds number is small. The basic set of equations for Stokesian hydrodynamics can be derived from the Onsager variational principle (Doi 2011, 2013). The main ideas are outlined as follows.

From the experimental observations, we find the meniscus profile can be described by two variables, the height of capillary rise $h(t)$ and contact angle $\theta(t)$. The time evolution of the system, described by the time derivatives $\dot{h}$ and $\dot{\theta}$, is determined by the minimum condition of the function

$$\mathcal{R}(h, \theta, \dot{h}, \dot{\theta}) = \Phi(h, \theta, \dot{h}, \dot{\theta}) + \frac{\partial A}{\partial h}\dot{h} + \frac{\partial A}{\partial \theta}\dot{\theta}, \qquad (4.1)$$

where $A(h, \theta)$ is the free energy of the system, and $\Phi(h, \theta, \dot{h}, \dot{\theta})$ is the free-energy dissipation function, which is defined as one half of the rate of free-energy dissipation in the fluid when the meniscus evolves at rates $\dot{h}$ and $\dot{\theta}$. Since the fluid flow obeys the Stokesian dynamics, Φ is a quadratic function of $\dot{h}$ and $\dot{\theta}$ in the linear response regime.
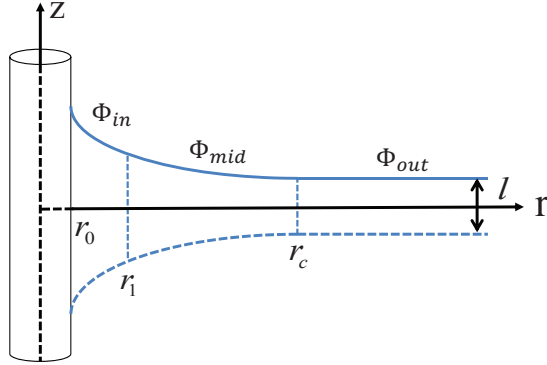
FIGURE 13. Cylindrical coordinate system $(r, \phi, \hat{z})$ used in the theoretical analysis of the soap film dynamics. The origin of the coordinate system is taken at the intersection of the fiber axis and mid-plane of the soap film of thickness ℓ. The total free-energy dissipation Φ in the soap film contains three contributions, $\Phi = \Phi_{in} + \Phi_{mid} + \Phi_{out}$, where Φ_{in} is from the inner region $(r_0 < r \leq r_1)$, Φ_{mid} is from the middle region $(r_1 < r \leq r_c)$ and Φ_{out} is from the outer region $(r > r_c)$.

The minimum condition of Eq. (4.1),

$$\frac{\partial \Phi}{\partial \dot{h}} + \frac{\partial A}{\partial h} = 0$$
$$\frac{\partial \Phi}{\partial \dot{\theta}} + \frac{\partial A}{\partial \theta} = 0,$$
(4.2)

represents the force balance between two kinds of forces, the hydrodynamic frictional force $\partial \Phi / \partial \dot{h}$ (or $\partial \Phi / \partial \dot{\theta}$) and reversible force $f_1 = -\partial A / \partial h$ (or $f_2 = -\partial A / \partial \theta$) in the generalized coordinates. The above variational principle can be derived directly from the basic equations of Stokesian hydrodynamics. It can also be regarded as a special form of the Onsager variational principle, which governs the time evolution of non-equilibrium systems characterized by a set of slow variables in the linear response regime (Doi 2011, 2013). This method as an analysis tool has been applied recently to a range of problems (Doi 2015; Man & Doi 2016; Xu, Di & Doi 2016; Di, Xu & Doi 2016).

We now use Eq. (4.2) to derive the dynamic equations of $h(t)$ and $\theta(t)$. For the convenience of theoretical treatment, we use a cylindrical coordinate system $(r, \phi, \hat{z})$, as shown in Fig. 13. The soap film is symmetric with respect to the vertical $\hat{z}$ axis. The cylindrical coordinates $(r, \hat{z})$ used here are related to the coordinates (x, z) used in the previous sections through $r = r_0 + x$ and $\hat{z} = \ell/2 + z$. Here $r_0 = d/2$ is the radius of the fiber and ℓ is the thickness of the soap film.

The meniscus profile is described by a function $\hat{z} = \hat{z}(r)$. We assume that $\hat{z}(r)$ is still given by Eq. (3.1), but a modification is needed. According to Eq. (3.1), $\hat{z}$ decreases continuously with increasing r, but in reality, $\hat{z}(r)$ is limited by the film thickness ℓ. We thus assume that the meniscus profile is governed by the following equation

$$\hat{z}(r; t) = \begin{cases} H(r; t) & r \leq r_c(t) \\ \ell/2 & r > r_c(t), \end{cases}$$
(4.3)

where $H(r; t)$ is given by

$$H(r; t) = \frac{\ell}{2} + h(t) - r_0 \cos \theta(t) \ln \left[\frac{r + [r^2 - r_0^2 \cos^2 \theta(t)]^{1/2}}{r_0 \cos \theta(t))} \right],$$
(4.4)

in agreement with Eq. (3.1), and $r_c(t)$ is determined by

$$H(r_c(t); t) = \frac{\ell}{2}. \tag{4.5}$$

Since the change in ℓ is small in the experiment, we consider ℓ as a constant in our analysis. For the convenience of later analysis, the meniscus profile is also represented by r as a function of $\hat{z}$, given by

$$r = R(\hat{z}) = r_0 \cos \theta(t) \cosh \left[\frac{h(t) + \ell/2 - \hat{z}}{r_0 \cos \theta(t)} \right], \tag{4.6}$$

for $r \leq r_c(t)$.

4.2. *Temporal evolution of the height of capillary rise* $h(t)$

To derive the governing equations of $h(t)$ and $\theta(t)$ with the Onsager principle, we need to calculate the free energy A and free-energy dissipation function Φ of the system. In this section, we briefly present our calculations with more details given in Appendix.

We first consider the free energy A. Since the *vertical* length scale of the system is much smaller than the capillary length λ_c, one can ignore the gravitational energy and calculate the free energy A of the system as a sum of the interfacial energy between the fiber and liquid, denoted by A_{fiber}, and the surface energy of the liquid film, denoted by A_{film}. They are given by the function $H(r)$ as

$$A_{fiber} \simeq -2\pi \gamma r_0 \tilde{h}, \tag{4.7}$$

$$A_{film} = \pi \gamma \left(2 \int_{r_0}^{r_c} \sqrt{1 + (\partial_r H)^2} \, r dr - r_c^2 \right). \tag{4.8}$$

where $\tilde{h} = H(r_0) = h + \ell/2 - r_0 \cos \theta \ln[(1 + \sin \theta)/\cos \theta]$. In the above equations, we have assumed that the fiber is completely wetted by the fluid with $\cos \theta \simeq 0$.

As the contact angle θ in the experiment is small, we can compute the energies by ignoring higher-order contributions of θ. The details are given in Appendix B. For A_{fiber}, we have

$$A_{fiber} \approx -2\pi \gamma r_0 (h + \frac{\ell}{2}).$$

For A_{film}, we have

$$A_{film} \approx \pi \gamma (r_0^2 \ln \frac{r_c}{r_0} - r_0^2).$$

Using the relation between h and r_c (see Eq. (A 4) in Appendix A), we have

$$A_{film} \approx \pi \gamma r_0 (h - r_0 \ln 2 - r_0).$$

Therefore, the reversible force f_1 is given by

$$f_1 = -\frac{\partial A}{\partial h} = -\frac{\partial A_{film}}{\partial h} - \frac{\partial A_{fiber}}{\partial h} \approx \pi r_0 \gamma. \tag{4.9}$$

It is interesting to note that $\partial A_{fiber}/\partial h \approx -2\partial A_{film}/\partial h$, so that the resulting generalized (capillary) force f_1 is a half of the local capillary force $f \simeq 2\pi r_0 \gamma$ [see Eq. (2.1)] acting on the CL without including the effect of the free energy penalty owing to the area increase of the liquid-air interface.

Next we consider the free-energy dissipation function Φ. As shown in Fig. 13, the total free-energy dissipation in the soap film contains three contributions, $\Phi = \Phi_{in} + \Phi_{mid} +$

Φ_{out}, where Φ_{in} is from the inner region $(r_0 < r \leq r_1)$, Φ_{mid} is from the middle region $(r_1 < r \leq r_c)$ and Φ_{out} is from the outer region $(r > r_c)$. Here r_1 is of the same order of magnitude as r_0, but the final result is not affected by the choice of r_1, as will be shown below. In the inner region $(r_0 < r \leq r_1)$, the free-energy dissipation arises mainly from the flow near the CL. When the CL moves at velocity $\dot{h}$, the dissipation function Φ_{in} in the inner region has the form (de Gennes *et al.* 2004)

$$\Phi_{in} \approx \frac{1}{2}\xi_{in}\dot{h}^2 = \frac{3\pi r_0 \eta \ln \varepsilon}{\theta}\dot{h}^2, \tag{4.10}$$

where ξ_{in} is given in Eq. (1.1).

In the outer region $(r > r_c)$, the soap film has a constant thickness ℓ. The fluid velocity is determined by the total inward flux $\tilde{a}$ flowing across any circular section of the soap film with a constant r. The flux $\tilde{a}$ is related to the change of the fluid volume V_{meni} in the region $r \leq r_c$:

$$\tilde{a} = \frac{dV_{meni}}{dt}. \tag{4.11}$$

Direct computation leads to

$$\tilde{a} = \pi r_0 r_c \dot{r}_c \approx \pi r_c^2 \dot{h}, \tag{4.12}$$

with more details given in Appendix C. Then the radial velocity of the fluid is given by

$$u_r = \frac{\tilde{a}}{2\pi r(\ell/2)} = \frac{r_c^2 \dot{h}}{r\ell}. \tag{4.13}$$

The free-energy dissipation function in the outer region is given by

$$\Phi_{out} = 2\pi\eta \int_{r_c}^{R_\infty} \left[(\partial_r u_r)^2 + \left(\frac{u_r}{r}\right)^2\right]\frac{\ell}{2}rdr \approx \frac{\pi r_c^2 \eta}{\ell}\dot{h}^2, \tag{4.14}$$

where R_∞ is the outer radius of the soap film, which is assumed to be much larger than r_c.

In the middle region $(r_1 < r \leq r_c)$, the radial velocity u_r is determined by the equation for volume conservation:

$$\frac{\partial H}{\partial t} = -\frac{1}{r}\frac{\partial}{\partial r}\left(rH(r)u_r\right), \tag{4.15}$$

in which u_r satisfies the boundary condition

$$u_r(r_c) = \frac{\tilde{a}}{2\pi r_c(\ell/2)} = \frac{r_c \dot{h}}{\ell}.$$

Integrating Eq. (4.15) leads to

$$u_r = \frac{1}{rH(r)}\left(\frac{r_c^2 \dot{h}}{2} + \int_r^{r_c} r\frac{\partial H}{\partial t}dr\right) = \frac{\dot{h}}{rH}\left(r_c^2 - \frac{r^2}{2}\right), \tag{4.16}$$

with the help of the relation $\partial H/\partial t \approx \dot{h}$ (see Eq. (A 2) in Appendix A). Then the dissipation function in the middle region is obtained as

$$\Phi_{mid} = 2\pi\eta \int_{r_1}^{r_c} \left[(\partial_r u_r)^2 + \left(\frac{u_r}{r}\right)^2\right]H(r)rdr \approx \frac{\pi\eta r_0 r_c^2}{\ell^2}\dot{h}^2, \tag{4.17}$$

with more details given in Appendix C.

Combining the above dissipation functions, we have the total free-energy dissipation

function

$$\Phi = \frac{3\pi r_0 \eta \ln \varepsilon}{\theta} \dot{h}^2 + \pi r_0 \eta \left(\frac{r_c^2}{\ell^2}\right) \dot{h}^2 + \pi r_c \eta \left(\frac{r_c}{\ell}\right) \dot{h}^2. \qquad (4.18)$$

Since ℓ is very small, it is assumed that $(\ell/r_c)^2 \ll \theta \ll 1$. Then the leading order of the dissipation function is

$$\Phi \simeq \frac{\pi r_0 \eta r_c^2}{\ell^2} \dot{h}^2, \qquad (4.19)$$

from the middle region $(r_1 < r \le r_c)$.

Using Eqs. (4.19), (4.9) and (4.2), we have

$$\frac{2r_c^2}{\ell^2} \dot{h} = \frac{\gamma}{\eta}, \qquad (4.20)$$

with $\dot{h}$ being smaller than the capillary speed γ/η by a factor of $(\ell/r_c)^2 \ll 1$. Using $r_c \approx r_0 \cosh(h/r_0)$ (see Eq. (A 7) in Appendix A), we have

$$r_c^2 \approx r_0^2 \cosh^2(h/r_0) \approx (r_0^2/4) \exp(2h/r_0). \qquad (4.21)$$

Equation (4.20) then becomes

$$\frac{r_0^2}{\ell^2} \exp\left(\frac{2h}{r_0}\right) \dot{h} = \frac{2\gamma}{\eta}, \qquad (4.22)$$

and its solution is given by

$$h = \frac{r_0}{2} \ln(4\Gamma t + 4c_0), \qquad (4.23)$$

where $\Gamma = (\gamma/\eta r_0)(\ell/r_0)^2 \equiv \Gamma_0(\ell/r_0)^2$ is a rate coefficient and c_0 is a constant determined by the initial condition. Note that for thick films with $\ell > 2r_0$, the rate coefficient scales as $\Gamma_0 = \gamma/\eta r_0$. For thin films considered here, the rate coefficient is reduced by a factor of $(\ell/r_0)^2 \ll 1$, compared with that for thick films.

Equation (4.23) states that the height of capillary rise $h(t)$ for a thin liquid film increases logarithmically in time t. This is much slower than the standard capillary rise for a bulk fluid, in which the height $h(t)$ increases as a power law of t (Quéré, Di Meglio & Brochard-Wyart 1988; Clanet & Quéré 2002). The slow capillary rise of the thin film along a vertical fiber is caused by the fact that the liquid flow inside the soap film is subjected to a severe confinement over a large area $(\sim \pi r_c^2)$. This flow thus involves a large viscous dissipation in the middle region of the soap film, which slows down the capillary rise. For a bulk fluid without confinement, however, the viscous dissipation of the flow occurs mainly in the inner region near the CL, which is more localized and less dissipative.

The solid lines in Fig. 10 show the fits of Eq. (4.23) to the two sets of data obtained from two soap film systems. It is seen that the two data sets are well described by Eq. (4.23) with two fitting parameters, c_0 and Γ. The black circles are fit with $c_0 = 7.19$ and $\Gamma = 0.60$ (black line), and red triangles are fit with $c_0 = 1.82$ and $\Gamma = 0.05$ (red line).

4.3. *Friction on a hanging fiber*

It is shown in Eq. (4.18) that the total free-energy dissipation Φ in the soap film contains contributions from three regions. Correspondingly, the total friction coefficient ξ_{tot}, which is defined by the equation $\Phi \equiv (1/2)\xi_{tot}\dot{h}^2$, can be written as $\xi_{tot} = \xi_{in} + \xi_{mid} + \xi_{out}$, where ξ_{in}, ξ_{mid} and ξ_{out} are, respectively, the contributions from the inner, middle and outer regions. From the above derivations, one can ready show that the dimensionless

friction coefficient in the middle region goes as, $\xi_{mid}/(2\pi r_0 \eta) = (r_c/\ell)^2 \simeq (\gamma/r_0\eta)t$, for large values of t. Similarly, in the outer region we find $\xi_{out}/(2\pi r_0\eta) \simeq (\ell/r_0)(\gamma/r_0\eta)t$ for large values of t. For typical values of $\gamma/r_0\eta \sim 10^7 \ s^{-1}$ (see introduction), $t \sim 100$ s (see Fig. 12), and $\ell/r_0 \sim 10^{-2}$ (see discussions on Fig. 14 below) used in the experiment, we find $\xi_{mid}/(2\pi r_0\eta) \gtrsim 10^9$ and $\xi_{out}/(2\pi r_0\eta) \gtrsim 10^7$, which are too large to be excited by a vertically oscillating thin fiber (see Fig. 14 below). As a result, the hanging fiber probe only feels the viscous damping caused by the fluid in the inner region of the soap film, with which it has a direct contact. The measured friction coefficient ξ_s, as shown in Fig. 12, is therefore directly related to the energy dissipation Φ_{in} associated with the fluid motion near the CL, which is given by Eq. (4.10).

From Eq. (4.10), we have the relation

$$\xi_{in}\dot{h} = 2\frac{\partial \Phi_{in}}{\partial \dot{h}}, \tag{4.24}$$

where the factor 2 accounts for the two menisci on the upper and lower sides of the soap film. The friction coefficient ξ_{in} is given by

$$\xi_{in}(t) = \frac{12\pi r_0 \eta \ln \varepsilon}{\theta(t)}, \tag{4.25}$$

where the time-dependence of $\xi_{in}(t)$ results from the temporal evolution of the dynamic contact angle $\theta(t)$. To calculate the temporal evolution of $\theta(t)$ using Eq. (4.2), one needs to consider higher order terms ($h.o.t.$) to the free energy A and dissipation function Φ (i.e., beyond $\theta \approx 0$).

The computation for the free energy A is relatively easy (see Eq. (B 3) in Appendix B). Using the formula for A, we obtain

$$f_2 = -\frac{\partial A}{\partial \theta} \approx \pi\gamma r_0^2(\frac{h}{r_0} - 1)\theta - \pi\gamma r_0^2\theta^2 + h.o.t. \tag{4.26}$$

The computation for the free-energy dissipation function Φ, however, is more involved. In Appendix C, we compute the higher-order contributions to the dissipation function and obtain [see Eq. (C 13)]

$$\Phi \approx \frac{\pi\eta r_0 r_c^2}{\ell^2}(\dot{h} + \alpha r_0\theta\dot{\theta})^2, \tag{4.27}$$

where $\alpha = h/r_0 - \tanh(h/r_0) \approx h/r_0 - 1$. Using Eqs. (4.2), (4.26) and (4.27), we have

$$\frac{2\pi\eta\alpha r_0^2 r_c^2\theta}{\ell^2}(\dot{h} + \alpha r_0\theta\dot{\theta}) = \pi\gamma r_0^2(\frac{h}{r_0} - 1)\theta - \pi\gamma r_0^2\theta^2. \tag{4.28}$$

Using Eq. (4.20) for $\dot{h}$, we find that the first-order terms in θ cancel out and Eq. (4.28) becomes

$$\frac{2\eta r_0 r_c^2}{\ell^2}\left(\frac{h}{r_0} - 1\right)^2\dot{\theta} = -\gamma.$$

Equivalently,

$$\dot{\theta} = -\frac{\gamma\ell^2}{2\eta(h/r_0 - 1)^2 r_0 r_c^2} = -\frac{\dot{h}/r_0}{(h/r_0 - 1)^2}, \tag{4.29}$$

where Eq. (4.20) is used again. This leads to

$$\theta(t) = c_{\theta 0} + \frac{1}{h/r_0 - 1} = c_{\theta 0} + \left(\frac{1}{2}\ln(4\Gamma t + 4c_0) - 1\right)^{-1}, \tag{4.30}$$

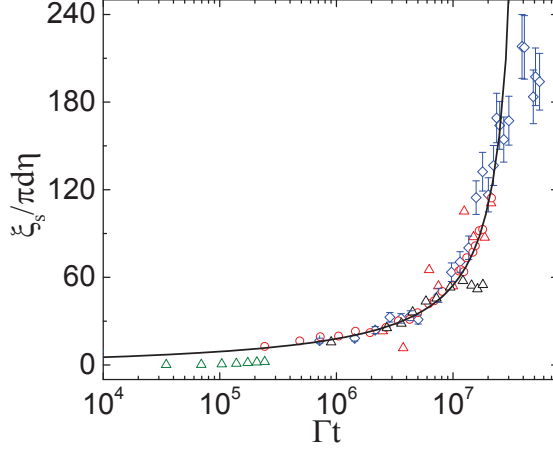where $c_{\theta 0}$ is a constant to be determined by the initial value of θ, and the last equality

FIGURE 14. Scaling plot of the normalized sidewall friction coefficient $\xi_s/\pi d\eta$ as a function of the normalized fiber draining time Γt for the five sets of data shown in Fig. 12. The color code used here is the same as that in Fig. 12. The solid line shows a fit of Eq. (4.33) to the data points with the fitting parameters $\epsilon = 1.105$, $c_\theta 0 = -0.118$ and $c_0 = 1.8$.

of Eq. (4.30) is obtained using Eq. (4.23). From Eqs. (4.25) and (4.30), we find

$$\xi_{in} = \frac{12\pi r_0 \eta \ln \varepsilon}{c_{\theta 0} + \left((1/2) \ln(4\Gamma t + 4c_0) - 1 \right)^{-1}}. \tag{4.31}$$

We now compare the theoretical prediction with the experiment. According to Eq. (4.31), the normalized friction coefficient $\xi_{in}/(\pi d\eta)$ is a universal function of Γt for all the soap film systems with different values of fiber diameter $d \ (= 2r_0)$, film viscosity η, film thickness ℓ and surface tension γ. Figure 14 is a scaling plot of the experimental data shown in Fig. 12. In this plot, the vertical axis is the normalized sidewall friction coefficient $\xi_s/(\pi d\eta)$, where $\xi_s(t)$ is defined as

$$\xi_s(t) \equiv \Delta\xi(t) - \xi_c = \xi(t) - \xi_a - \xi_c. \tag{4.32}$$

In the above, $\xi(t)$ is measured total friction coefficient, ξ_a is the friction coefficient measured in air and ξ_c is the friction coefficient of the two contact lines given in Eq. (3.4). The horizontal axis is the normalized fiber draining time Γt with Γ being the rate coefficient given in Eq. (4.23). From the AFM force measurement, we estimate the film thickness ℓ of the red circles to be approximately $\ell \simeq 20 \ nm$. With this value of ℓ and the known values of d, η and γ, we calculate the value of Γ for the red circles. For all other sets of data, we use Γ (or equivalently ℓ) as a fitting variable to scale the data horizontally. It is seen from Fig. 14 that all the data sets can be collapsed on to a single master curve, once Γt is used as the scaling variable. The fitted values of Γ and the corresponding values of ℓ are given in Table 1. The obtained values of ℓ are all in the expected range of the film thickness.

To further test the functional form of the obtained master curve in Fig. 14, we rewrite Eq. (4.31) as

$$\frac{\xi_{in}}{2\pi r_0 \eta} = \frac{6 \ln \varepsilon}{c_{\theta 0} + \left((1/2) \ln[4(\Gamma t + c_0)] - 1 \right)^{-1}}. \tag{4.33}$$

The solid line in Fig. 14 shows a fit of Eq. (4.33) to the data points with ε, $c_{\theta 0}$ and c_0 as three fitting parameters. It is seen that the experimental data are well described by

TABLE 1. Five soap film samples used in the experiment with different values of fiber diameter d and soap film viscosity η. The surface tension of all the soap films is $\gamma = 23.2\ mN/m$. The obtained values of the fitting parameter Γ used in the scaling plot shown in Fig. 14 and the corresponding values of the film thickness ℓ are listed in the 5th and 6th columns, respectively.

Samples	Symbol	d (μm)	η (cP)	$\Gamma(s^{-1})$	ℓ (nm)
1	△	2.6	1.65	20808	56.90
2	◇	2.6	1.65	12138	43.46
3	○	1.1	13.7	4048	20
4	△	2.6	13.7	1445	43.30
5	△	1.75	1.65	26.76	15028

Eq. (4.33). From the fitted value of the parameters, we find $\theta(t) = 0.011$ (or $0.63°$) when $\Gamma t = 10^7$. As shown in Eq. (1.1), the value of ε in the wedge-shaped region away from the CL is expected to be $\varepsilon \simeq R/a$ (de Gennes *et al.* 2004), where $R = r_1 \simeq 2r_0$ is the upper cut-off length of the inner range and a ($\simeq 1$ nm) is the lower cut-off length away from the moving CL. With the average value of fiber radius $r_0 = 1.065\ \mu m$ used for the five samples shown in Table 1, we have $\xi_{in}/(2\pi r_0 \eta) \simeq 46/\theta(t)$ ($\simeq 4180$ when $\Gamma t = 10^7$), which is about 70 times larger than the measured value.

In deriving Eq. (4.33) [and Eq. (1.1)], one has assumed that there is a relative motion between the solid surface and liquid layer in the entire inner range until the distance z away from the moving CL reaches the lower cut-off length a ($\simeq 1$ nm). This assumption, however, is not valid for an oscillating fiber used in the experiment. When the fiber oscillates along its long axis with a angular frequency ω_0, the viscous shear wave can only penetrate into a thin fluid layer of thickness $\delta = (2\nu/\omega_0)^{1/2}$ from the fiber surface (Landau & Lifshitz 1986), where $\nu = \eta/\rho$ is the kinematic viscosity. This layer of fluid will oscillate in phase with the fiber, contributing only an added mass and no dissipation to the oscillating fiber. For liquids with $\eta \gtrsim 1$ cP and $\omega_0 \simeq 2\pi \times 120$ kHz, we have $\delta \gtrsim 1.6\ \mu m$. Consequently, the cut-off length a, above which the hydrodynamic friction becomes relevant, is increased considerably. If one sets $a = 1.6\ \mu m$, the value of $\ln \varepsilon$ in Eq. (4.33) becomes $\ln \varepsilon \simeq \ln(2.13/1.6) \simeq 0.286$, which is approximately 30 times smaller than the typical value of $\ln \varepsilon$ with $a \simeq 1$ nm. This estimated value of $\varepsilon \simeq 1.33$ is very close to the fitted value of $\epsilon = 1.105$ and thus explains the fitting results shown in Fig. 14. The above discussion suggests that the Brownian motion of the glass fiber itself introduces a new lower cut-off length a, which prevents the viscous dissipation from being divergent at the zero contact angle limit.

There is an additional frequency-dependent friction coefficient ξ_{ac}, resulting from the vertical oscillation of the glass fiber at the angular frequency ω_0 (Landau & Lifshitz 1986; Xiong *et al.* 2009). It was shown that ξ_{ac} takes the form (Xiong *et al.* 2009; Guo *et al.*, 2013)

$$\xi_{ac} \simeq 2\pi\eta h \left(\frac{r_0}{\delta}\right) = \pi\eta r_0 \left(\frac{r_0}{\delta}\right) \ln(4\Gamma t + 4c_0), \tag{4.34}$$

where Eq. (4.23) was used to obtain the second equality in Eq. (4.34). We compute the value of ξ_{ac} with the experimental parameters given in Table 1 and find it is approximately 10 times smaller than the frequency-independent friction coefficient ξ_{in} given in Eq. (4.31). Therefore, the contribution from ξ_{ac} is ignored in the fitting shown in Fig. 14.

5. Conclusion

We have carried out a combined experimental and theoretical study of the confinement effect of thin soap films in the dynamics of spreading along a vertical micron-sized glass fiber. In the experiment, we built an optical imaging system to monitor the development of the meniscus of a freely suspended soap film in the vicinity of the vertical glass fiber as a function of fiber draining time t after it pierces through the soap film at $t = 0$. For a thin soap film with its thickness ℓ being smaller than the fiber diameter d, we find the soap film creeps slowly along the glass fiber during the entire observation time up to hours. The speed of the creeping flow along the glass fiber depends sensitively on the film thickness ℓ when it is in the thin film regime ($\ell \lesssim d$). The shape of the evolving film meniscus is found to have a similar functional form as the equilibrium profile given in Eq. (3.1) with a time-dependent height of capillary rise $h(t)$ on the fiber surface. The slow dynamics of thin film spreading varies logarithmically with time t [i.e., goes as $\ln(\Gamma t)$] at the long-time limit, which is different from the power-law relaxation as described by Tanner's law for spreading of an unconfined fluid near a moving CL. Such a logarithmic relaxation is also observed in the measured viscous friction coefficient $\xi_s(t)$ felt by the glass fiber in contact with a soap film, when the film creeps slowly along the glass fiber with a decreasing contact angle $\theta(t)$.

To explain the observed time-dependence of the height of capillary rise $h(t)$ and friction coefficient $\xi_s(t)$ of the soap film, we used the Onsager variational principle and obtained the equations of motion to describe the dynamics of two important parameters in thin film spreading, namely, the height of capillary rise $h(t)$ and contact angle $\theta(t)$. The newly derived equations of motion provide the analytical solutions of $h(t)$ and $\theta(t)$, which are found to be in good agreement with the experimental results. It is shown that the height of capillary rise $h(t)$ reaches its equilibrium value logarithmically in time t at the long-time limit [i.e., $h(t) \sim \ln(\Gamma t)$]. The relaxation rate Γ for a thin film is given by $\Gamma \simeq \Gamma_0[\ell/(d/2)]^2$, where Γ_0 is the relaxation rate for spreading of an unconfined fluid along a fiber and the factor $[\ell/(d/2)]^2$ is caused by the confinement effect of the thin film. It is also shown that the normalized friction coefficient, $\xi_s/(\pi d\eta) \sim 1/\theta(t)$, is a universal function of Γt. Indeed, the values of $\xi_s/(\pi d\eta)$ obtained under different experimental conditions, such as different values of fiber diameter d, film viscosity η, film thickness ℓ and surface tension γ, are found to collapse on to a master curve, once they are plotted as a scaling function of Γt, which was varied by more than three decades. The successful application of the Onsager variational principle to the problem of thin film spreading allows us to have a better understanding of the confinement effect of thin films in the dynamics of spreading along a fiber. Such a understanding is relevant to many industrial processes, such as coating on fibrous materials and development of new functional materials (Duprat *et al.* 2012).

Appendix A. Approximation of some geometric parameters

Following the experimental observations, the meniscus profile is given by Eq. (4.4). We now derive approximations for some geometric parameters of the soap film with the assumption that θ is small. First, to the leading order, Eq. (4.4) can be written as

$$\hat{z} = H(r, t) \approx h(t) + \frac{\ell}{2} - r_0 \ln\left(\frac{r + \sqrt{r^2 - r_0^2}}{r_0}\right). \tag{A 1}$$

This implies that

$$\frac{\partial H}{\partial t} \approx \dot{h}, \tag{A 2}$$

and

$$\frac{\partial H}{\partial r} \approx -\frac{r_0}{r}, \tag{A 3}$$

when $r \gg r_0$. Noticing that $H(r_c) = \ell/2$ and $r_c \gg r_0$, we have

$$h(t) \approx r_0 \ln\left(\frac{r_c + \sqrt{r_c^2 - r_0^2}}{r_0}\right) \approx r_0 \ln\left(\frac{2r_c}{r_0}\right) = r_0\left[\ln\left(\frac{r_c}{r_0}\right) + \ln 2\right]. \tag{A 4}$$

This equation implies that

$$\dot{h} \approx \frac{r_0}{r_c}\dot{r}_c, \qquad \text{or equivalently,} \qquad \dot{r}_c \approx \frac{r_c}{r_0}\dot{h}. \tag{A 5}$$

Second, from Eq. (4.6), we have

$$r = R(\hat{z}) \approx r_0 \cosh\left(\frac{h + \ell/2 - \hat{z}}{r_0}\right). \tag{A 6}$$

This equation implies that

$$r_c = R\left(\frac{\ell}{2}\right) = r_0 \cosh\left(\frac{h}{r_0}\right). \tag{A 7}$$

It is easy to see that Eqs. (A 4) and (A 7) are equivalent in the leading order approximation.

Appendix B. Approximation of surface energies

The total surface energy of the system includes two parts, namely, the surface energy on the fiber A_{fiber} and surface energy of the liquid film A_{film}:

$$A_{fiber} = -2\pi\gamma r_0 \tilde{h}, \tag{B 1}$$

$$A_{film} = \pi\gamma\left(2\int_{r_0}^{r_c} \sqrt{1 + (\partial_r H)^2}\, r\, dr - r_c^2\right). \tag{B 2}$$

Here $\tilde{h} = H(r_0) = h + \ell/2 - r_0 \cos\theta \ln((1 + \sin\theta)/\cos\theta)$. In A_{fiber}, we ignore a constant term, $2\pi r_0 \gamma_{SV} L$, with γ_{SV} and L being, respectively, the surface energy density and total length of the fiber. In A_{film}, we ignore a constant term, $\pi\gamma R_\infty^2$, with R_∞ being the outer radius of the soap film.

Leading order approximation. Suppose that θ and ℓ are small. We retain the leading order term and ignore the higher order terms. For A_{fiber}, we have

$$A_{fiber} = -2\pi\gamma r_0\left(h + \frac{\ell}{2} - r_0 \cos\theta \ln\frac{1 + \sin\theta}{\cos\theta}\right) \approx -2\pi\gamma r_0 h.$$

For A_{film}, we have

$$A_{film} = \pi\gamma\left(2\int_{r_0}^{r_c}\sqrt{1+(\partial_r H)^2}rdr - r_c^2\right) \approx \pi\gamma\left(2\int_{r_0}^{r_c}\left(1+\frac{(\partial_r H)^2}{2}\right)rdr - r_c^2\right)$$

$$= \pi\gamma\left(\int_{r_0}^{r_c}(\partial_r H)^2rdr - r_0^2\right) \approx \pi\gamma(r_0^2\ln\frac{r_c}{r_0} - r_0^2).$$

Higher order approximation. Further calculations are needed to compute the higher order terms in the expression of the free energy. Direct calculations of the total surface energy $A = A_{fiber} + A_{film}$ give [see Eqs. (B 1) and (B 2)],

$$A = \pi\gamma\left(r_c\sqrt{r_c^2 - r_0^2\cos^2\theta} - r_c^2 + (h - \frac{\ell}{2})r_0\cos\theta - 2hr_0\right.$$

$$\left.+ r_0^2(2-\cos\theta)\ln\frac{1+\cos\theta}{\sin\theta} - r_0^2\sin\theta\right). \tag{B 3}$$

Since $\theta \ll 1$ and $\exp(\frac{h}{r_0}) \gg 1$, we have

$$\frac{\partial A}{\partial\theta} \approx \pi\gamma r_0^2(\frac{h}{r_0} - 1)(\cosh(\frac{2h}{r_0}) - \sinh(\frac{2h}{r_0}) - 1)\theta + \pi\gamma r_0^2\theta^2 + h.o.t.$$

$$\approx -\pi\gamma r_0^2(\frac{h}{r_0} - 1)\theta + \pi\gamma r_0^2\theta^2 + h.o.t. \tag{B 4}$$

Appendix C. Approximation of energy dissipation functions

Dissipation function in the outer region $(r > r_c)$. Since the thickness ℓ of the soap film does not change much, we know, by volume conservation, that the total inward flux at any circular section is constant and is given by

$$\tilde{a} = \frac{dV_{meni}}{dt}, \tag{C 1}$$

where V_{meni} denotes the volume of the liquid under the meniscus. Direct computations give

$$V_{meni} = 2\pi\int_{r_0}^{r_c}H(r)rdr = \frac{\pi}{2}\left(r_0r_c\sqrt{r_c^2 - r_0^2} - r_0^2h + \ell(r_c^2 - \frac{r_0^2}{2})\right) \approx \frac{\pi}{2}r_0r_c^2. \tag{C 2}$$

This leads to

$$\tilde{a} = \pi r_0r_c\dot{r}_c \approx \pi r_c^2\dot{h}, \tag{C 3}$$

where we have used Eq. (A 5). The velocity in the r direction is a function of r and is given by

$$u_r = \frac{\tilde{a}}{\pi r\ell}. \tag{C 4}$$

The energy dissipation function in this region is given by

$$\Phi_{out} = 2\pi\eta\int_{r_c}^{R_\infty}\left((\partial_r u_r)^2 + (\frac{u_r}{r})^2\right)\frac{\ell}{2}rdr$$

$$= 2\pi\eta\int_{r_c}^{R_\infty}\frac{\tilde{a}^2}{\pi^2r^3\ell}dr = \frac{\tilde{a}^2}{\pi r_c^2\ell} \approx \frac{\pi r_c^2\eta}{\ell}\dot{h}^2, \tag{C 5}$$

where R_∞ is the outer radius of the soap film, which is assumed to be much larger than r_c.

Dissipation function in the middle region $(r_1 < r \le r_c)$. We assume that the fluid velocity has a radial component $u_r(r)$ only. By volume conservation, we have

$$\frac{\partial H}{\partial t} = -\frac{1}{r}\frac{\partial}{\partial r}(rH(r)u_r). \tag{C 6}$$

Noticing the boundary condition

$$u_r(r_c) = \frac{\tilde{a}}{\pi r \ell}.$$

Direct calculations give

$$u_r = \frac{1}{rH(r)}\Big(\frac{\tilde{a}}{2\pi} + \int_r^{r_c} r\frac{\partial H}{\partial t}dr\Big) = \frac{\dot{h}}{rH}(r_c^2 - \frac{r^2}{2}). \tag{C 7}$$

Here we have used Eqs. (A 2) and (C 3). This leads to

$$\partial_r u_r = -\frac{\dot{h}}{r^2 H(r)}(r_c^2 + \frac{r^2}{2}) + \frac{\dot{h}}{rH(r)^2}(r_c^2 - \frac{r^2}{2})\frac{r_0}{r}.$$

Here we have used Eq. (A 3). Near the boundary $r = r_c$, the height of the meniscus is close to $\ell/2$, so that the $H(r)^{-2}$ term dominates. In the leading order, we have

$$\partial_r u_r \approx \frac{\dot{h}}{rH(r)^2}(r_c^2 - \frac{r^2}{2})\frac{r_0}{r}. \tag{C 8}$$

Then the energy dissipation function in the leading order is given by

$$\Phi_{mid} = 2\pi\eta\int_{r_1}^{r_c} rH(r)\Big((\partial_r u_r)^2 + (\frac{u_r}{r})^2\Big)dr \approx 2\pi\eta r_0^2\dot{h}^2\int_{r_1}^{r_c}\frac{(r_c^2 - r^2/2)^2}{r^3 H(r)^3}dr. \tag{C 9}$$

We set $z = H(r)$, using the relation $r \approx r_0\cosh(\frac{h-z}{r_0})$ and $r_c \approx r_0\cosh(\frac{h-\ell/2}{r_0})$, and change the variable of integration, and finally we obtain

$$\Phi_{mid} = 2\pi\eta r_c^2 r_0\dot{h}^2\int_{\ell/2}^{h_1}\frac{(\cosh^2((h-\ell/2)/r_0) - \cosh^2((h-z)/r_0)/2)^2}{z^3\cosh^2((h-z)/r_0)\cosh^2((h-\ell/2)/r_0)}dz$$

$$\approx \frac{\pi\eta r_0 r_c^2}{\ell^2}\dot{h}^2. \tag{C 10}$$

Higher order approximation of the dissipation function. From the analysis in the previous section, we have shown that the energy dissipation is dominated by that in the middle region. Here we compute the higher order terms of the energy dissipation function in the middle region. As in (C 2), the total volume in the inner and middle regions is given by

$$V_{meni} \approx \frac{\pi}{2}r_0 r_c^2 = \frac{\pi r_0^3}{2}\cosh^2(\frac{h-\ell/2}{r_0\cos\theta}).$$

Here we have used the relation $r_c = r_0\cosh(\frac{h-\ell/2}{r_0\cos\theta})$. Direct computations give the flux

$$\tilde{a} = \frac{dV_{meni}}{dt} \approx \pi r_c^2(\dot{h} + \alpha r_0\theta\dot{\theta}), \tag{C 11}$$

with $\alpha = \frac{h}{r_0} - \tanh\frac{h}{r_0}$. This equation differs from Eq. (C 1) only by a higher order term of θ. Similar analysis as in the previous section leads to

$$\Phi_{mid} = \frac{\pi\eta r_0 r_c^2}{\ell^2}(\dot{h} + \alpha r_0\theta\dot{\theta})^2. \tag{C 12}$$

This implies that the total energy dissipation function,

$$\Phi \approx \Phi_{mid} = \frac{\pi \eta r_0 r_c^2}{\ell^2} (\dot{h} + \alpha r_0 \theta \dot{\theta})^2. \qquad (C\,13)$$

REFERENCES

BONN, D., EGGERS, J., INDEKEU, J., MEUNIER, J. & ROLLEY, E. 2009 Wetting and spreading. *Rev. Mod. Phys.* **81**, 739.

CLANET, C. & QUÉRÉ, D. 2002 Onset of menisci. *J. Fluid Mech.* **460**, 131-149.

DECKER, E. L. & GAROFF, S. 1997 Contact Angle Hysteresis: The Need for New Theoretical and Experimental Models. *J. Adhesion* **63**, 159.

DE GENNES, P. G., BROCHARD-WYART, F. & QUÉRÉ, D. 2004 *Capillarity and Wetting Phenomena: Drops, Bubbles, Pearls, Waves* (Springer, New York, USA).

DE GENNES, P. G. 1985 Wetting: statics and dynamics. *Rev. Mod. Phys.* **57**, 827.

DI, Y., XU, X., &DOI M. 2016 Theoretical analysis for meniscus rise of a liquid contained between a flexible film and a solid wall. *Europhys. Lett.* **113**, 36001.

DOI, M. 2013 *Soft Matter Physics* (Oxfort University Press).

DOI, M. 2011 Onsager's variational principle in soft matter. *J. Phys. Condens. Matter* **23**, 284118.

DOI, M. 2015 Onsager principle as a tool for approximation. *Chinese Phys. B* **24**, 020505.

DUPRAT, C., PROTIERE, S., BEEBE, A. Y., & STONE, H. A. 2012 Wetting of flexible fibre arrays *Nature* **482**, 510-513.

DUSSAN, E. B. V. & DAVIS, S. H. J. 1974 On the motion of a fluid-fluid interface along a solid surface. *Fluid Mech.* **65**, 71.

GUAN, D., WANG, Y. J., CHARLAIX, E. & TONG, P. 2016a Asymmetric and speed-dependent capillary force hysteresis and relaxation of a suddenly stopped moving contact line. *Phys. Rev. Lett.* **116**, 066102.

GUAN, D., WANG, Y. J., CHARLAIX, E. & TONG, P. 2016b Simultaneous observation of asymmetric speed-dependent contact force hysteresis and slow relaxation of a suddenly stopped moving contact line. *Phys. Rev. E* **94**, 042802.

GUO, S., GAO, M., XIONG, X., WANG, Y., WANG, X., SHENG, P., & TONG, P. 2013 Direct measurement of friction of a fluctuating contact line. *Phys. Rev. Lett.* **111**, 026101.

GUO, S., XIONG, X., XU, Z., SHENG, P., & TONG, P. 2014 Measurement of the friction coefficient of a fluctuating contact line using an AFM-based dual-mode mechanical resonator. *Chin. Phys. B* **23**, 116802.

GUO, S., LEE, C. H., SHENG, P. & TONG, P. 2015 Measurement of contact-line dissipation in a nanometer-thin soap film. *Phys. Rev. E* **91**, 012404.

HUIBERS, P. D. T. & SHAH, D. O. 1997 Multispectral determination of soap film thickness. *Langmuir* **13**, 5995-5998.

KAZ, D. M., MCGORTY R., MANI M., BRENNER, M. P. & MANOHARAN, V. N. 2012 Physical ageing of the contact line on colloidal particles at liquid interfaces. *Nature Materials* **11**(2), 138-142.

LANDAU, L. D. & LIFSHITZ, E. M. Fluid Mechanics (Butterworth-Heinemann, Oxford, 1986), 2nd ed.

LEGER, L. & JOANNY, J.-F. 1992 Liquid spreading. *Rep. Prog. Phys.* **55**, 431.

LOEWENBERG, M. 1993 The unsteady Stokes resistance of arbitrarily oriented, finitelength cylinders. *Phys. Fluid A* **5**, 3004.

MA, H., JIMENEZ, J., & RAJAGOPALAN, R. 2000 Brownian Fluctuation Spectroscopy Using Atomic Force Microscopes. *Langmuir* **16** , 2254-2261.

MAN, X. & DOI, M. 2016 Ring to Mountain Transition in Deposition Pattern of Drying Droplets. *Phys. Rev. Lett.* **116**, 066101.

PAGONABARRAGA, I. 2012 Adsorbed colloids relax slowly. *Nature Materials* **11**(2), 99-100.

POULIN, P., NALLET, F., CABANE, B. & BIBETTE, J. 2015 Evidence for Newton black films between adhesive emulsion droplets. *Phys. Rev. Lett.* **77**, 3248-3251.

Quéré, D., Di Meglio, J.& Brochard-Wyart, F. 1988 Wetting of fibers : theory and experiments. *Revue de Physique Applique* **23**, 1023.

Quéré, D.. 2008 Wetting and roughness *Annu. Rev. Mater. Res.* **38**, 71.

Ramiasa, M., Ralston, J., Fetzer, R. & Sedev, R. 2014 The influence of topography on dynamic wetting. *Adv. Colloid Interface Sci.* **206**, 275.

Snoeijer, J. H. & Andreotti, B. 2013 Moving Contact Lines: Scales, Regimes, and Dynamical Transitions. *Annu. Rev. Fluid Mech.* **45**, 269.

Tanner, L. H. 1979 The spreading of silicone oil drops on horizontal surfaces. *Journal of Physics D: Applied Physics* **12** , 1473.

Wang, Y.-J., Guo, S., Chen, H.-Y. & Tong, P. 2016 Understanding contact angle hysteresis on an ambient solid surface *Phys. Rev. E* **93**, 052802.

Xiong, X., Guo, S., Xu, Z., Sheng, P., & Tong, P. 2009 Development of an atomic-force-microscope-based hanging-fiber rheometer for interfacial microrheology. *Phys. Rev. E* **80**, 061604.

Xu, X., Di, Y. & Doi, M. 2016 Variational method for liquids moving on a substrate. *Phys. Fluids* **28**, 087101.

Yazdanpanah, M. M., Hosseini, M., Pabba, S., Berry, S. M., Dobrokhotov, V. V., Safir, A., Keynton, R. S. & Cohn, R. W. 2008 Micro-Wilhelmy and Related Liquid Property Measurements Using Constant-Diameter Nanoneedle-Tipped Atomic Force Microscope Probes. *Langmuir* **24**, 13753.